



Research Paper

A phenomenological model of the synapse between the inner hair cell and auditory nerve: Implications of limited neurotransmitter release sites

Ian C. Bruce^{a,*}, Yousof Erfani^a, Muhammad S.A. Zilany^b

^a Department of Electrical & Computer Engineering, McMaster University, Hamilton, ON, Canada

^b Department of Computer Engineering, University of Hail, Hail, Saudi Arabia



ARTICLE INFO

Article history:

Received 2 August 2017

Received in revised form

11 December 2017

Accepted 23 December 2017

Available online 28 December 2017

Keywords:

Auditory model

Synapse

Neurotransmitter vesicle release

Spike timing statistics

Refractoriness

Renewal process

ABSTRACT

Peterson and Heil [Hear. Res., In Press] have argued that the statistics of spontaneous spiking in auditory nerve fibers (ANFs) can be best explained by a model with a limited number of synaptic vesicle docking (release) sites (~ 4) and a relatively-long average redocking time (~ 16 – 17 ms) for each of the sites. In this paper we demonstrate how their model can be: i) generalized to also describe sound-driven ANF responses and ii) incorporated into a well-established and widely-used model of the entire auditory periphery [Zilany et al., J. Acoust. Soc. Am. 135, 283–286, 2014]. The responses of the new model exhibit substantial improvement in several measures of ANF spiking statistics, and predicted physiological forward-masking and rate-level functions from the new model structure are shown to also better match published physiological data.

© 2017 Elsevier B.V. All rights reserved.

1. Introduction

In the mammalian ear, excitation of auditory nerve fibers (ANFs) is achieved via release of neurotransmitter contained in synaptic vesicles at the basolateral wall of inner hair cells (IHCs), as illustrated in Fig. 1. While this synapse shares many characteristics with other synapses in the mammalian nervous system, it also has some specializations that enable high firing rates and temporal precision in ANF spiking (see Safieddine et al., 2012, for a recent review). IHCs have specialized presynaptic zones with a presynaptic ribbon that helps traffic vesicles to the release sites. A number of proteins are thought to form the docking sites that facilitate exocytosis of the vesicles, although the exact location and form of the docking proteins in IHCs is still somewhat uncertain. The influx of calcium through voltage-dependent calcium channels provide the trigger for neurotransmitter release. The dynamics of this synaptic release process, along with the dynamics of the postsynaptic receptor channels and the intrinsic dynamics of action potential generation

in ANFs, will contribute to the spiking statistics of ANFs that lay the foundation for neural coding of sound.

Analyses of the statistics of action potentials from the first few decades of recording in single ANFs led to the widespread approach of modeling the spiking statistics as a renewal process, where the spiking probability is dependent on the time of the previous spike but not on the earlier history of spiking (e.g., Johnson and Swami, 1983). The renewal process that best described the data was a Poisson process modified by a recovery process that takes into account the refractory properties of ANFs (e.g., Johnson and Swami, 1983; Li and Young, 1993). A Poisson process produces exponentially distributed intervals between events, and refractoriness reduces the chances of obtaining short interspike intervals (ISIs). The Poisson statistics (before refractoriness) could arise from a large number of synaptic vesicle docking sites at the presynaptic membrane, each with a small probability of release. The recovery process is normally split into an absolute refractory period, where no spikes can occur, and a relative refractory period, where the discharge probability is reduced.

Some analyses have suggested two time scales for the relative refractoriness of ANFs (Gaumond et al., 1982, 1983; Li and Young, 1993), leading Carney (1993) to include a double-exponential refractory recovery (with time constants of 0.8 and 25 ms) in her

* Corresponding author.

E-mail addresses: ibruce@ieee.org (I.C. Bruce), erfani.yousof@gmail.com (Y. Erfani), msazilany@gmail.com (M.S.A. Zilany).

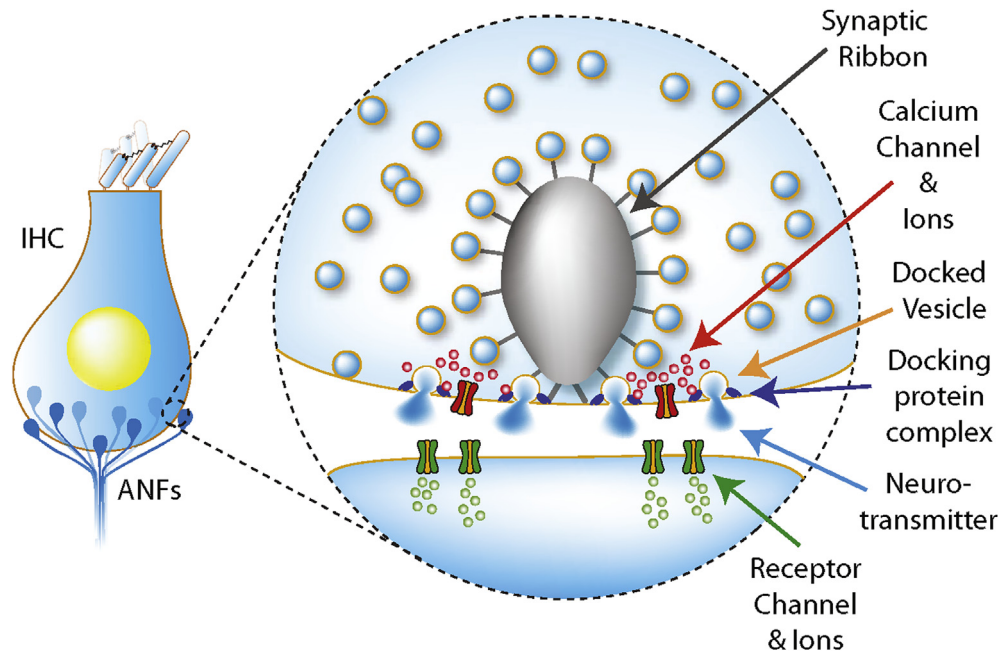


Fig. 1. Illustration of the inner hair cell (IHC) to auditory nerve fiber (ANF) synapse. Note that there may only be a limited number of vesicle docking sites formed by docking protein complexes from which neurotransmitter can be released across the synaptic cleft. After exocytosis of a vesicle, it may take some time for a new vesicle to be transported from the synaptic ribbon to the empty docking site. Similarly, after redocking it may take some time for another vesicle on the ribbon to be brought into proximity with the docking sites. Note that the depiction of the docking sites is for illustration only—the exact location and form of the docking proteins in IHCs is still somewhat uncertain (e.g., see Safieddine et al., 2012). Adapted with permission by R. Nouvian from <http://www.inmfrance.com/inm/fr/audition/90-lar-determinants-of-hair-cell-exocytosis>.

influential model of the auditory periphery. These time constants were changed to 1 and 12.5 ms in the next version of the model (Zhang et al., 2001) and retained in all the subsequent models in the series (Heinz et al., 2001; Bruce et al., 2003; Tan and Carney, 2003; Zilany and Bruce, 2006, 2007; Zilany et al., 2009, 2014).

However, analyses of the refractory properties of ANFs electrically stimulated from a cochlear implant, and thus bypassing the inner hair cell (IHC) synapse onto the ANF, have not shown evidence of any refractory component with a time constant on the order of 12.5–25 ms (Cartee et al., 2000, 2006; Miller et al., 2001). Furthermore, a number of studies have now demonstrated that ANFs have fractal rather than renewal properties, where the spiking probability fluctuates over time and depends on the long-term history of spike times (Teich and Khanna, 1985; Teich, 1989; Teich et al., 1990; Lowen and Teich, 1992; Peterson et al., 2014). The fluctuation over time was incorporated into the Zilany et al. (2009, 2014) auditory periphery models as a fractional Gaussian noise (fGn; Jackson and Carney, 2005) in the presynaptic adaptation section of the model, which could be caused by channel noise in voltage-gated ion channels of the IHC (Moezzi et al., 2014, 2016). However, the spike generation section of Zilany et al. (2009, 2014) is a renewal process with double-exponential relative refractory recovery, as stated above.

Peterson et al. (2014) have argued that the longer component of the recovery process could actually be due to a smaller number of synaptic vesicle docking sites and depression of the release probability due to depletion of docked vesicle. Moezzi et al. (2014), also investigated the action of presynaptic depression in their version of the Meddis (2006) model but had a shorter depression time and a larger number of release sites than did Peterson et al. (2014), and Moezzi et al. (2014) did not differentiate between long and short components of the recovery process. Peterson and Heil (In Press) reformulated their deterministic model of Peterson et al. (2014) into a probabilistic model, making it suitable for incorporation into the phenomenological auditory periphery model of Zilany et al.

(2009, 2014). However, the model of Peterson and Heil (In Press) focussed on the spontaneous activity of ANFs and thus did not incorporate the adaptation properties required to describe sound-evoked ANF responses.

In this paper we: i) describe how the model of Peterson and Heil (In Press) can be generalized to sound-driven activity including adaptation effects, ii) derive analytical estimates of the mean and variance in firing rate for this synapse-ANF model, and iii) demonstrate how the modified synapse model produces improved predictions of a number of sets of published ANF data.

2. Model structure and computational implementation

Fig. 2A shows a schematic of the phenomenological model of the auditory periphery. The input is a sound-pressure wave at the eardrum and the output is simulated spike times from an ANF with a given characteristic frequency (CF). The old and new synapse and spike generator model structures are compared in panels B and C, respectively, of Fig. 2. The modified model structure and parameter values were adjusted based on model predictions of the published physiological data given in the Results section and the Supplementary Material. In addition, we ran further simulations (not shown) to confirm that other response properties that were optimized in previous versions of the model were not compromised by the modifications.

The new model considers the case of 4 synaptic vesicle docking sites for exocytosis (see Fig. 1), as was found by Peterson et al. (2014) and Peterson and Heil (In Press) to best explain the statistics for spontaneous activity in ANFs. Peterson et al. (2014) and Peterson and Heil (In Press) proposed a fixed mean time for an empty docking site to be replenished with a new vesicle (which we will refer to as “redocking” in this article) in the range 13.5–17 ms. This fixed mean redocking time can produce the rapid (~2 ms) exponential adaptation implemented previously in the auditory-periphery model by the Westerman and Smith (1988)

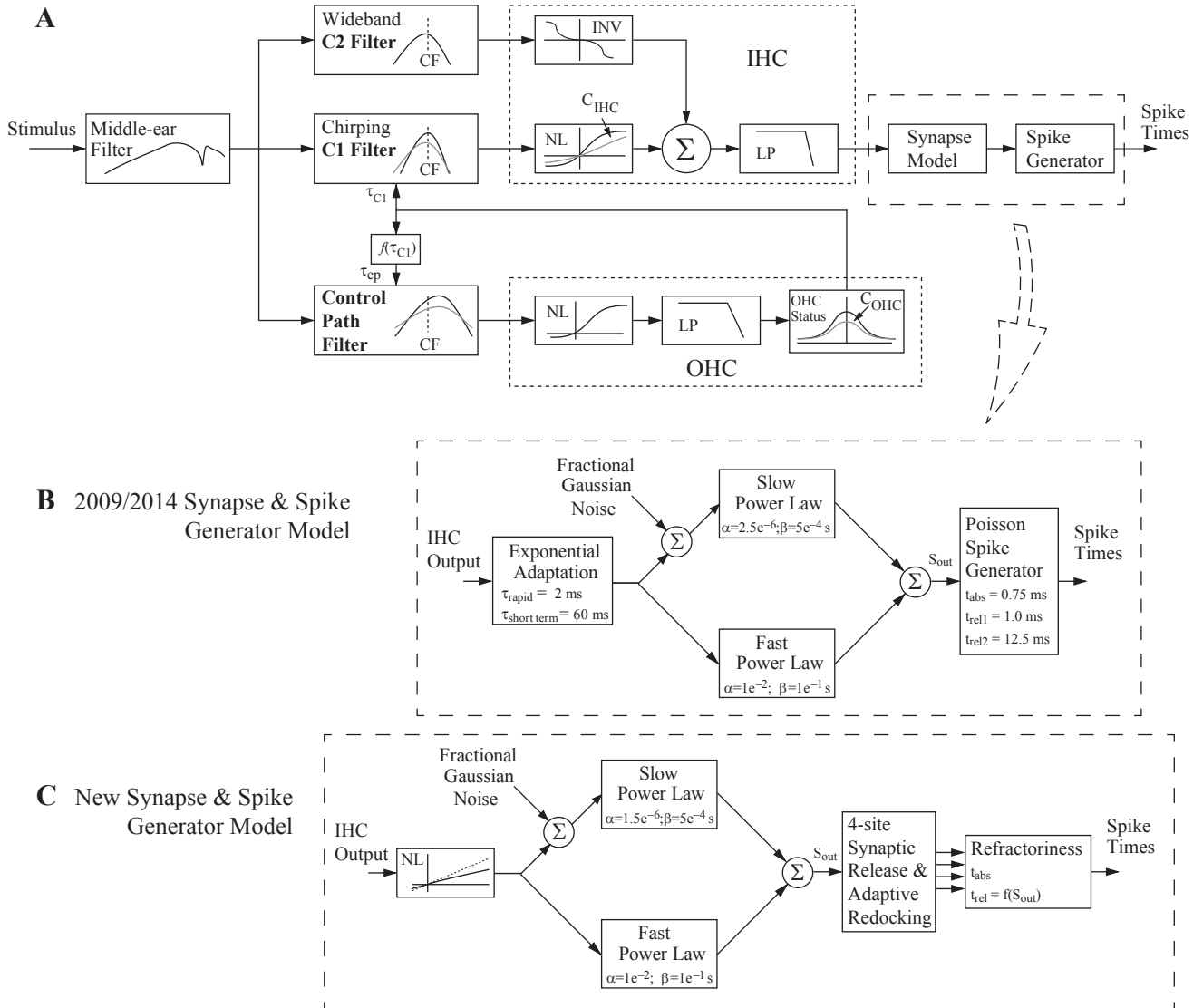


Fig. 2. **A** Schematic of the overall structure of the model of the mammalian auditory periphery from Zilany et al. (2009, 2014), which is retained in the new model. **B** IHC-ANF synapse and spike-generation model structure from the 2009/2014 version of the model. **C** Proposed new structure of the synapse and spike-generation model. Abbreviations: outer hair cell (OHC), inner hair cell (IHC), low-pass (LP) filter, static nonlinearity (NL), characteristic frequency (CF), and inverting nonlinearity (INV). Panels A & B adapted from Zilany et al. (2009) with permission from the Acoustical Society of America (© 2009).

exponential adaptation model (see Fig. 2B) but not the short-term (~60 ms) adaptation component.

Thus, in the new model, an adaptive redocking mechanism is implemented, which allows for the removal of the Westerman and Smith (1988) model from its previous location before the power-law adaptation (PLA) model, replaced with a gently-saturating nonlinearity (compare panels B and C of Fig. 2). In order to give a physiologically-realistic dependence of ANF threshold on CF and spontaneous rate (SR), the saturating nonlinearity is dependent on both of these model parameters and is given by:

$$\text{PLA}_{\text{in}} = \text{sign}(V_{\text{iHC}}) \times 10^{(0.9 \times \log_{10}(|V_{\text{iHC}} \times \text{CF}_{\text{factor}}|) + \text{MULT}_{\text{factor}})} + 3 \times \text{SR}, \quad (1)$$

where PLA_{in} represents the input to the power-law adaptation function and has units of /s, V_{iHC} denotes the IHC's relative transmembrane potential in units of V, CF has units of Hz, and SR has units of /s. In order to provide the correct ANF spontaneous firing

rate, the constant term of $3 \times \text{SR}$ is included in the mapping function, the output of which is subjected to power-law adaptation. It was found that, for the current set of power-law parameters, this constant term produced the correct spontaneous rate ($\approx \text{SR}$) at the ANF spike output. Also, incorporating this constant term before the PLA provides the desired adaptation response at the offset of a stimulus, which is characterized by a pause followed by the slow recovery to the spontaneous rate. Note that the fGn in the slow PLA path prevents the spontaneous rate from continuously adapting down to a value of zero. The two factors, $\text{CF}_{\text{factor}}$ and $\text{MULT}_{\text{factor}}$, are determined according to:

$$\text{CF}_{\text{slope}} = \text{SR}^{0.19} \times 10^{-0.87}, \quad (2)$$

$$\text{CF}_{\text{const}} = 0.1 \times (\log_{10}(\text{SR}))^2 + 0.56 \times \log_{10}(\text{SR}) - 0.84, \quad (3)$$

$$CF_{\text{sat}} = 10^{(8.9655 \times CF_{\text{slope}} + CF_{\text{const}})}, \quad (4)$$

$$CF_{\text{factor}} = 2 \times \min\left(CF_{\text{sat}}, 10^{\left(\frac{CF_{\text{slope}} \times CF_{\text{const}}}{1000} + CF_{\text{const}}\right)}\right), \quad (5)$$

$$MULT_{\text{factor}} = \max\left(4.3 - \frac{CF}{5000}, 2.95 \times \max\left(1, 1.5 - \frac{SR}{100}\right)\right). \quad (6)$$

Power-law adaptation describes an adaptation process that is scale invariant, i.e., it continues to adapt no matter the length of the stimulus rather than having fixed time constants (Drew and Abbott, 2006). Zilany et al. (2009) introduced PLA into their synapse model in order to obtain much improved predictions of ANF responses to on-going stimulation. In this paper, the amount of PLA has been adjusted by changing the parameter α (from 2.5×10^{-6} to 1.5×10^{-6}) in the slow power-law path to replicate the AN responses more accurately to forward-masking paradigms (Harris and Dallos, 1979).

To produce short-term adaptation (with a time constant of ~ 60 ms) in the new synapse model, an adaptive mean redocking time is implemented according to the dynamics:

$$\tau_{\text{rd}}[n+1] = \begin{cases} \tau_{\text{rd}}[n] + 0.4 \times 10^{-3} \cdot N_{\text{rd}}[n], & \text{if } N_{\text{rd}}[n] > 0, \\ \tau_{\text{rd}}[n] + \frac{14 \times 10^{-3} - \tau_{\text{rd}}[n]}{60 \times 10^{-3}} \Delta t, & \text{if } N_{\text{rd}}[n] = 0, \end{cases} \quad (7)$$

where $\tau_{\text{rd}}[n]$ has units of seconds, $N_{\text{rd}}[n]$ is the number of synaptic redocking events that have occurred during time step n , which has a duration of Δt seconds, and τ_{rd} is initialized to a value of $\tau_{\text{rd}}[0] = 13.6 \times 10^{-3} + 0.02 \times 10^{-3} \cdot SR$ seconds. The adaptation in the mean redocking time can be explained in terms of an increase in the mean redocking time occurring after a synaptic redocking event because the vesicle that has docked will need to be replaced at its previous position on the synaptic ribbon by a more distant vesicles (see Fig. 1), and a decay in the mean redocking time back toward the resting value if no redocking events occur.

The computational implementation of the synaptic release and redocking is as follows. For the j^{th} of N synaptic release sites, the time interval $T_{\text{rd},ij}$ from the i^{th} synaptic release to a vesicle redocking is modeled as an exponentially-distributed random number with mean $\tau_{\text{rd}}[n]$ where n corresponds to the time step of the i^{th} release. Synaptic release is driven by the output of the power-law adaptation stage, the variable $S_{\text{out}}(t)$, which determines the average synaptic release rate across all docking sites if they have docked vesicles at that time. Thus, the average rate of release at one site if it has a docked vesicle is $S_{\text{out}}(t)/N$. Therefore, the time from the last redocking to the next synaptic release at the j^{th} site is computed via numerical integration according to:

$$\int_{t_{ij} + T_{\text{rd},ij}}^{t_{i+1,j}} \frac{S_{\text{out}}(t)}{N} dt \geq e_{ij}, \quad (8)$$

where t_{ij} is the time of the i^{th} synaptic release for the j^{th} site, $t_{i+1,j}$ is the time of the next synaptic release on that site, and e_{ij} is an exponentially-distributed random number with a mean of 1.

Following Peterson et al. (2014) and Peterson and Heil (In Press), synaptic release from any of the N sites in time step n can generate an action potential in the model ANF as long as it is not in a refractory state. Peterson et al. (2014) and Peterson and Heil (In Press)

used a fixed absolute refractory period of 0.6 ms and an exponentially-distributed relative refractory period with a mean duration of 0.6 ms. However, the data of Miller et al. (2001) indicate that ANFs may each have different values for their absolute and relative refractory periods. Furthermore, the data of Li and Young (1993) indicate that the effective relative refractory period may be shorter for higher synaptic release rates, which would be consistent with multiple postsynaptic potentials being more likely to sum temporally to reach the elevated threshold potential observed during relative refractoriness.

Thus, in the new model t_{abs} can take a range of values uniformly distributed over the range [208.5 μ s, 691.5 μ s]. This range is based on the distribution from Miller et al. (2001), which is obtained by intracochlear electrical stimulation, but was scaled by a factor of 1.5. This scaling takes into account that electrical stimulation can lead to action potential generation on a range of nodes of Ranvier of an ANF, which can shorten the effective absolute refractory period, whereas for acoustic stimulation the action potential is thought to always occur at the node of Ranvier closest to the synapse from the IHC. Again based on the distribution from Miller et al. (2001), the baseline mean relative refractory period \tilde{t}_{rel} can take a range of values uniformly distributed over the range [131.0 μ s, 894.0 μ s]. Miller et al. (2001) did not report on whether the absolute and relative refractory period values were correlated in their data, but the computational models of Negm and Bruce (2014) and Boulet and Bruce (2017) suggest that voltage-gated ion channels in ANFs that influence refractoriness tend to have an effect on both the absolute and the relative refractory period. Therefore, in the new model we make these values fully correlated, i.e., a single uniformly-distributed pseudorandom is generated for each ANF and scaled according to the different distributions for t_{abs} and \tilde{t}_{rel} . To make the effective relative refractory period shorter for higher synaptic release rates, the mean relative refractory period for time step n is then computed according to:

$$t_{\text{rel}}[n] = \min\left\{\frac{K \tilde{t}_{\text{rel}}}{S_{\text{out}}[n]}, \tilde{t}_{\text{rel}}\right\}, \quad (9)$$

where the factor $K = 100$ /s (the same units as $S_{\text{out}}[n]$), such that $t_{\text{rel}}[n]$ and \tilde{t}_{rel} share the same units.

Fractional Gaussian noise is a generalization of the common white Gaussian noise process to include long-range temporal dependence (Jackson and Carney, 2005). Zilany et al. (2009) introduced fGn into their synapse model in order to describe the nonstationarity observed in the long-range firing rates of ANFs. Peterson and Heil (In Press) argued that the standard deviation of the fGn in the Zilany et al. (2009, 2014) model (see panels B and C of Fig. 2) should be reduced substantially. In this study we found it sufficient to reduce the fGn standard deviation to a value of 1 /s for low-spont fibers, 10 /s for medium-spont fibers and SR/2 /s for high-spont fibers. In the model of Zilany et al. (2009, 2014), the fGn was sufficient to explain the distribution of spont rates with just a single value of the parameter SR for each spont-rate class, i.e., high, medium and low. However, the reduction of the standard deviation of the fGn in the new model means that, to accurately predict the spont-rate histogram obtained from ANF recordings in cat, the

Table 1
Distributions of the parameter SR for the three spont-rate classes.

SR class	mean (/s)	std. (/s)	limits (/s)
Low	0.1	0.1	[1×10^{-3} , 0.2]
medium	4	4	[0.2, 18]
High	70	30	[18, 180]

value of SR for each ANF in the new model must be drawn from a Gaussian distribution with the means, standard deviations and limits for each of the three spont-rate classes as given in Table 1.

Model code is provided in the [Supplementary Material](#).

3. Analytical approximations of mean and variance in firing rate

In Zilany et al. (2014), analytical approximations were provided for the mean and variance in the firing rate, taking into consideration the effects of absolute refractoriness. Analytical approximations are helpful in uses of the model that require estimates of the mean and variance in firing rate, such as the application of signal detection theory to model neural activity to predict perceptual performance (e.g., Heinz et al., 2002), because obtaining reliable estimates of the mean and variance from the model's spike train outputs can require hundreds or thousands of trials. The spiking statistics are more complicated in the new model, but analytical approximations can still be derived if we consider the case where S_{out} , τ_{rd} and t_{rel} are constant.

Following a release event at the j^{th} of N docking sites, the redocking times $T_{rd,j}$ will be exponentially distributed with a mean redocking time of τ_{rd} , i.e.:

$$f_{T_{rd,j}}(t) = \begin{cases} 0, & \text{for } t < 0, \\ \frac{1}{\tau_{rd}} e^{-t/\tau_{rd}}, & \text{for } t \geq 0. \end{cases} \quad (10)$$

Following a redocking event at the j^{th} of N docking sites, release times T_{rl} for a total mean release rate of S_{out} divided equally between the N sites will be exponentially distributed according to:

$$f_{T_{rl,j}}(t) = \begin{cases} 0, & \text{for } t < 0, \\ \frac{S_{out}}{N} e^{-tS_{out}/N}, & \text{for } t \geq 0. \end{cases} \quad (11)$$

The distribution of intervals between synaptic release events at the j^{th} of N docking sites T_j can be obtained by convolving the exponential distributions for the redocking time $T_{rd,j}$ and the release time $T_{rl,j}$ to obtain:

$$f_{T_j}(t) = \begin{cases} 0, & \text{for } t < 0, \\ \frac{S_{out}}{S_{out}\tau_{rd} - N} \left\{ e^{-t/\tau_{rd}} - e^{-S_{out}t/N} \right\}, & \text{for } t \geq 0. \end{cases} \quad (12)$$

Note that while the above expression may appear to be undefined for $\tau_{rd} = N/S_{out}$, the limit of the expression as $\tau_{rd} \rightarrow N/S_{out}$ is $t e^{-t/\tau_{rd}}/\tau_{rd}^2$, corresponding to a gamma distribution with shape parameter 2, as noted by Peterson and Heil (In Press).

Peterson and Heil (In Press) refer to two different approaches to determining the distribution of intervals between release events T for the superposition of N renewal processes. While these two methods give equivalent distributions, the new method of Torab and Kamen (2001) gives a simpler expression for the general case of N processes (see Eq. (16) of Peterson and Heil, In Press) than does the older method of Cox and Smith (1954). However, in our methodology to incorporate the effects of refractoriness (described below), we have only been able to find a closed-form solution using the approach of Cox and Smith (1954) for specific values of N .

From Cox and Smith (1954), the superposition of N renewal processes described by (12) gives a distribution of intervals between release events T that can be found via:

$$f_T(t) = -\frac{d}{dt} \left\{ F_c(t) \left[\int_t^\infty \frac{F_c(x)}{E[T_j]} dx \right]^{N-1} \right\}, \quad (13)$$

where $F_c(t)$ is the complementary cumulative distribution function corresponding to the single-site distribution of T_j given by (12) and $E[T_j]$ is the mean time between release events at a single site.

From (12), the complementary cumulative distribution function of T_j is:

$$F_c(t) = 1 - \int_{-\infty}^t f_{T_j}(x) dx \quad (14)$$

$$= 1 - \frac{N - S_{out}\tau_{rd} - Ne^{-S_{out}t/N} + S_{out}\tau_{rd}e^{-t/\tau_{rd}}}{N - S_{out}\tau_{rd}} \quad (15)$$

$$= \frac{Ne^{-S_{out}t/N} - S_{out}\tau_{rd}e^{-t/\tau_{rd}}}{N - S_{out}\tau_{rd}}, \quad (16)$$

and the expected value for intervals between releases at the j^{th} of N docking sites is:

$$E[T_j] = \int_{-\infty}^{\infty} t f_{T_j}(t) dt \quad (17)$$

$$= \int_0^{\infty} t \cdot \frac{S_{out}}{S_{out}\tau_{rd} - N} \left\{ e^{-t/\tau_{rd}} - e^{-S_{out}t/N} \right\} dt \quad (18)$$

$$= \tau_{rd} + \frac{N}{S_{out}}. \quad (19)$$

Solving for (13) for the case of $N = 4$, given the expressions obtained in (16) and (19), the distribution of release-event intervals superimposed for the 4 docking sites is then:

$$f_T(t) = \left(\tau_{rd} + \frac{4}{S_{out}} \right)^{-3} \left(\frac{S_{out}}{4} - \frac{1}{\tau_{rd}} \right)^{-4} \left\{ 6e^{-t \left(\frac{S_{out}}{2} + \frac{2}{\tau_{rd}} \right)} \left(\frac{S_{out}}{4} + \frac{1}{\tau_{rd}} \right)^2 \right. \\ \left. + \frac{S_{out}^4 \tau_{rd}^2 e^{-\frac{4t}{\tau_{rd}}}}{64} + \frac{64e^{-S_{out}t}}{S_{out}^2 \tau_{rd}^4} - \frac{S_{out}^2 \tau_{rd}^2 e^{-t \left(\frac{S_{out}}{4} + \frac{3}{\tau_{rd}} \right)} \left(\frac{S_{out}}{4} + \frac{3}{\tau_{rd}} \right)^2}{16} \right. \\ \left. - \frac{16e^{-t \left(\frac{3S_{out}}{4} + \frac{1}{\tau_{rd}} \right)} \left(\frac{3S_{out}}{4} + \frac{1}{\tau_{rd}} \right)^2}{S_{out}^2 \tau_{rd}^2} \right\} \quad (20)$$

Note that the above expression does not capture the dependency of the inter-event distribution on the history of the process preceding the most recent synaptic release event. However, a renewal process approximation to the actual release-redocking process can be formed by drawing independent synaptic release intervals from this distribution. Because of the independence of the intervals, this approximation is not appropriate for describing the variability in spiking *within a spike train*, but it is accurate in describing the variability in spike counts *across spike trains* generated with the same values of S_{out} , τ_{rd} and t_{rel} (as will be

demonstrated in the Results section), such as is used in applications of analytical signal detection theory utilizing the model.

The effects of refractoriness on the distribution of ISIs can be approximated well by multiplying the distribution of superimposed release-event intervals with the cumulative distribution function for recovery from refractoriness and rescaling the distribution to have an area of 1. Because of the exponential form of the refractory period distribution, these operations can be achieved by convolving the distribution from (20) with the refractory period T_{ref} distribution:

$$f_{T_{\text{ref}}}(t) = \begin{cases} 0, & \text{for } t < t_{\text{abs}}, \\ \frac{1}{t_{\text{rel}}} e^{-(t-t_{\text{abs}})/t_{\text{rel}}}, & \text{for } t \geq t_{\text{abs}}. \end{cases} \quad (21)$$

Solving for the mean and variance of the refractory-modified ISIs gives:

$$E[\text{ISI}] = \frac{\tau_{\text{rd}}}{4} + t_{\text{abs}} + t_{\text{rel}} + \frac{1}{S_{\text{out}}} \quad (22)$$

and

$$\begin{aligned} \text{var}[\text{ISI}] = & \frac{6\tau_{\text{rd}}^2}{(S_{\text{out}}\tau_{\text{rd}} + 4)^3} - \frac{33\tau_{\text{rd}}^2}{8(S_{\text{out}}\tau_{\text{rd}} + 4)^2} - \frac{24\tau_{\text{rd}}^2}{(S_{\text{out}}\tau_{\text{rd}} + 4)^4} \\ & + \frac{729\tau_{\text{rd}}^2}{256(3S_{\text{out}}\tau_{\text{rd}} + 4)} - \frac{243\tau_{\text{rd}}^2}{256(S_{\text{out}}\tau_{\text{rd}} + 12)} + \frac{1}{S_{\text{out}}^2} + \frac{\tau_{\text{rd}}^2}{16} \\ & + t_{\text{rel}}^2. \end{aligned} \quad (23)$$

Also from [Cox and Smith \(1954\)](#), the mean of the ANF firing rate can then be obtained via:

$$E[\text{rate}] = \frac{1}{E[\text{ISI}]}, \quad (24)$$

and the mean of the spike count in a time bin of length Δt will then be:

$$E[\text{count}] = E[\text{rate}]\Delta t. \quad (25)$$

Because the process is non-Poissonian, the variance in spike count will depend on the size of the time bin Δt . For $\Delta t \rightarrow \infty$:

$$\text{var}[\text{rate}]_{\Delta t \rightarrow \infty} \approx \frac{\text{var}[\text{ISI}]}{E[\text{ISI}]^3}, \quad (26)$$

while for $\Delta t \rightarrow 0$, the variance approaches that of a Poisson process, i.e.,:

$$\text{var}[\text{rate}]_{\Delta t \rightarrow 0} \approx E[\text{rate}], \quad (27)$$

and for finite time bin sizes the variance will fall somewhere between these values. The variance of the spike count in a time bin of length Δt will then be:

$$\text{var}[\text{count}] = \text{var}[\text{rate}]\Delta t, \quad (28)$$

where $\text{var}[\text{rate}]$ is obtained from either (26) or (27), depending on the whether the time bin size is relatively long or relatively short.

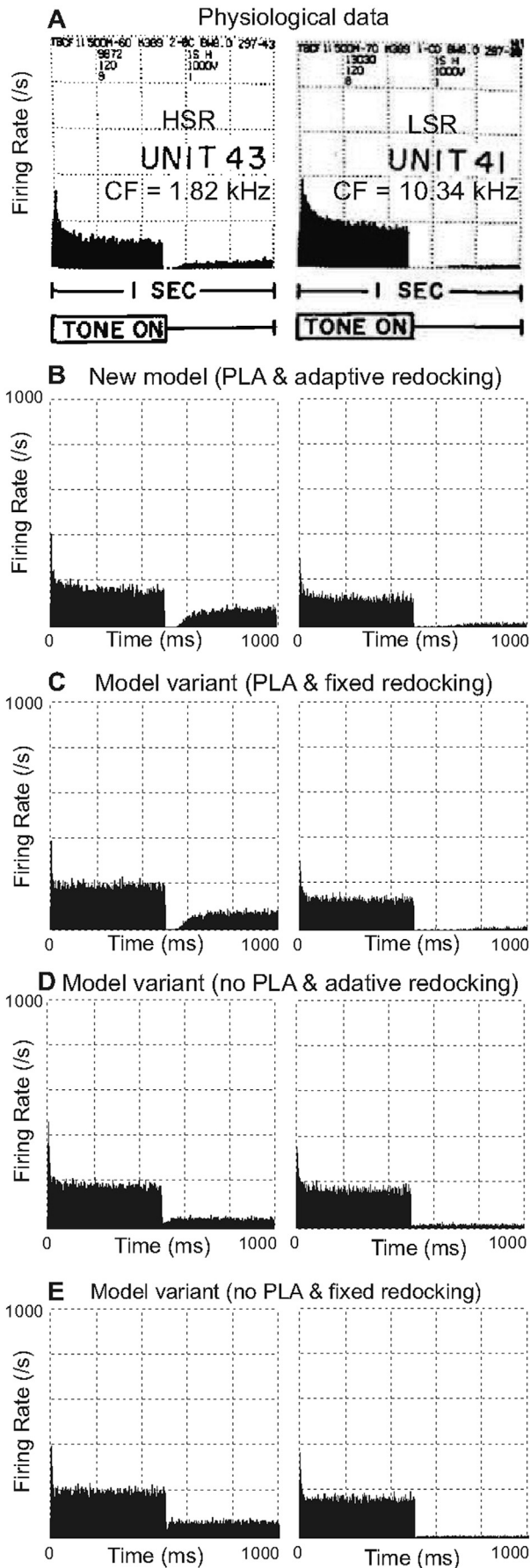
In addition to spike trains generated from the computational model described in the previous section, the provided code outputs values for (24) and (26) in each time bin n based on the values of $S_{\text{out}}[n]$, $\tau_{\text{rd}}[n]$, t_{abs} and $t_{\text{rel}}[n]$.

4. Results

Overall, the simulation results from this study exhibited equal or improved accuracy in predicting published ANF data compared to the results of [Zilany et al. \(2009, 2014\)](#). We first show that the onset and offset adaptation behavior of the new model is consistent with the published data and the previous model, despite the change in synapse model structure. We then show a series of simulation results for cases where there were substantial improvements achieved by the new model. Additional comparisons between published data and model predictions are provided in the Supplementary Material.

In response to a brief tonal stimulus, ANFs exhibit an onset response that decays with rapid (2 ms time constant) and a short-term (60 ms time constant) adaptation towards a steady-state response, as illustrated by the peri-stimulus time histograms (PSTHs) of the two example cat ANFs in [Fig. 3A](#). At the offset of the stimulus, the response drops below the spontaneous firing rate (often to a rate of zero spiking) before returning gradually back to the spont rate. Even with the change in the synapse model structure from the 2009/2014 model, the adaptation behavior is relatively similar (cf. [Fig. 5 of Zilany et al., 2009](#)). It was found in [Zilany et al. \(2009\)](#) that the double-exponential adaptation of the Westerman and Smith model could explain the rapid and short-term onset adaptation but power-law adaptation (PLA) is required to predict the depth and time-course of the offset adaptation. In the new model, power-law adaptation is still required to predict offset adaptation—compare panels B and C (models with PLA) of [Fig. 3](#) with panels D and E (models without PLA). In regards to the onset adaptation, both the PLA and the adaptive redocking contribute to the short-term onset adaptation component. A model variant with the mean redocking period fixed at 16 ms (rather than adaptive) and lacking PLA (panel E) shows an abrupt drop from the peak of the onset response to the steady-state, corresponding to an absence of a short-term (~60 ms) adaptation component. Adding in PLA but keeping the redocking fixed produces a more realistic short-term onset adaptation components for the low-spont model fiber (right-hand plot of panel C) but not for the high-spont model fiber (left-hand plot of panel C). A short-term adaptation component is more evident in both high-spont and low-spont model variants with adaptive redocking but no PLA (panel D), but the most physiologically-realistic time courses for the PSTHs are obtained with PLA and adaptive redocking (panel B).

An important aspect of ANF adaptation is its behavior in response to change in the amplitude in an ongoing stimulus. [Fig. 4](#) provides a comparison of gerbil ANF data from [Westerman and Smith \(1987\)](#) and predictions from the new model for the case of increments in the amplitude of an ongoing tonal stimulus. PSTHs for the gerbil data are shown in panel A, while PSTHs for the model are shown in panel B. In each subpanel, the stimulus has a different initial (or “background”) level (given in dB re. the fiber's threshold), and 300 ms after the stimulus onset the level is stepped up to 43 dB (re. threshold). It can be observed that the lowest initial level (10 dB) produces a small initial onset response but a large onset response to the increment. As the initial level increases, the initial onset response grows in amplitude, and there is a corresponding decrease in the amplitude of the onset response to the increment at 300 ms. This behavior is also produced by the new model (panel B). This conservation of the total onset response (the sum of initial and increment responses) is quantified in panels C (data) and D (model) by fitting each onset response of the PSTH with a function with two exponential components and a steady-state component. The firing rates of the fitted exponentials are multiplied by their time constants to give what Westerman and Smith refer to as the “integrated transient response components”. The subpanels of C and D



show the integrated responses for the rapid component of the onset (~ 2 ms time constant) and for the short-term component (~ 60 ms time constant). In both the data and the new model, a trade-off between the initial (background) onset response and the increment onset response is observed such that the total response for both the rapid and the short-term components of the onset remains fairly constant as a function of the initial level. Again, even with the change in the synapse model structure from the 2009/2014 model, this conservation in the adaptation for the increment paradigm is relatively similar to the previous version of the model (cf. Fig. 8 of Zilany et al., 2009). Model variants with a fixed (rather than adaptive) redocking mechanism or without PLA exhibit poorer predictions of the physiological behavior for the short-term adaptation component, as shown in panels E and F, respectively, of Fig. 4. PLA is required to obtain the conservation behavior for the longer term components of the onset response in this increment paradigm, but without the adaptive redocking mechanism (panel E), there is no component of the PSTH with a time constant of around 60 ms, and thus the fits for the short-term component are somewhat unreliable and the conservation behavior is not observed. Conversely, when adaptive redocking is included but PLA is excluded, the short-term adaptation component of the PSTH is more reliable, but the conservation behavior is weakened by the lack of PLA. Note that the goodness of the double-exponential fits to the PSTHs were also generally poorer for these model variants. No results are shown for the no-PLA & fixed redocking variant of the model because it produced such poor fits to the double-exponential function that the short-term component gave spurious values.

An important consequence of the PLA observed in Zilany et al. (2009) was that powerlaw adaptation can explain forward masking effects in ANFs while exponential adaptation cannot. As shown by the published data of Harris and Dallos (1979) plotted in Figs. 5A and 6A, ANFs can exhibit very long-lasting forward masking that grows very strongly with the level of the masker, such that masking effects can extend out past the longest measured masker-probe delay of 300 ms. As indicated by the gray curves in Figs. 5B and 6B, while the 2014 model with PLA does reasonably well at describing the forward masking simulation results for lower masker levels, it underestimates the strength and time-course of masking and how these depend on the masker level. The maximal strength of forward masking is somewhat constrained in the 2009/2014 model because of the Westerman and Smith (1988) double-exponential adaptation stage being placed *before* the PLA (see panel B of Fig. 2). This is due to the Westerman and Smith (1988) model strongly saturating in response to maskers presented at high levels, limiting how much further adaptation of the masker response occurs in the PLA stage. In contrast, with the new model having only a gently-saturating nonlinearity before the PLA stage (see panel C of Fig. 2) and the double-exponential adaptation shifted to the adaptive redocking mechanism after the PLA, the new model (black curves in Figs. 5B and 6B) is able to much more closely follow the properties of forward masking observed in the data.

As described in Section 2, the standard deviation of the fGn in the PLA section of the 2009/2014 model was set to fairly high values for each spont rate class (low-, medium-, and high-spont). This

Fig. 3. Comparison of adaptation in PSTHs for two cat ANFs and model predictions in response to 500-ms duration constant-amplitude stimuli, presented once a second over 2 min. Left panels: CF = 1.82 kHz, high-spont rate (unit 43 in data); right panels: CF = 10.34 kHz, low-spont rate (unit 41 in data). A: Data reprinted from Kiang (1965), with permission from MIT Press (© 1965). B: New model predictions for stimulus at 25 dB re. threshold for each model fiber (left subpanel: high spont; right subpanel low spont). C: Predictions for model variant with *fixed* redocking ($t_{rd} = 16$ ms) rather than adaptive redocking. D: Predictions for model with adaptive redocking but *no* PLA. E: Predictions for model with fixed redocking *and* no PLA.

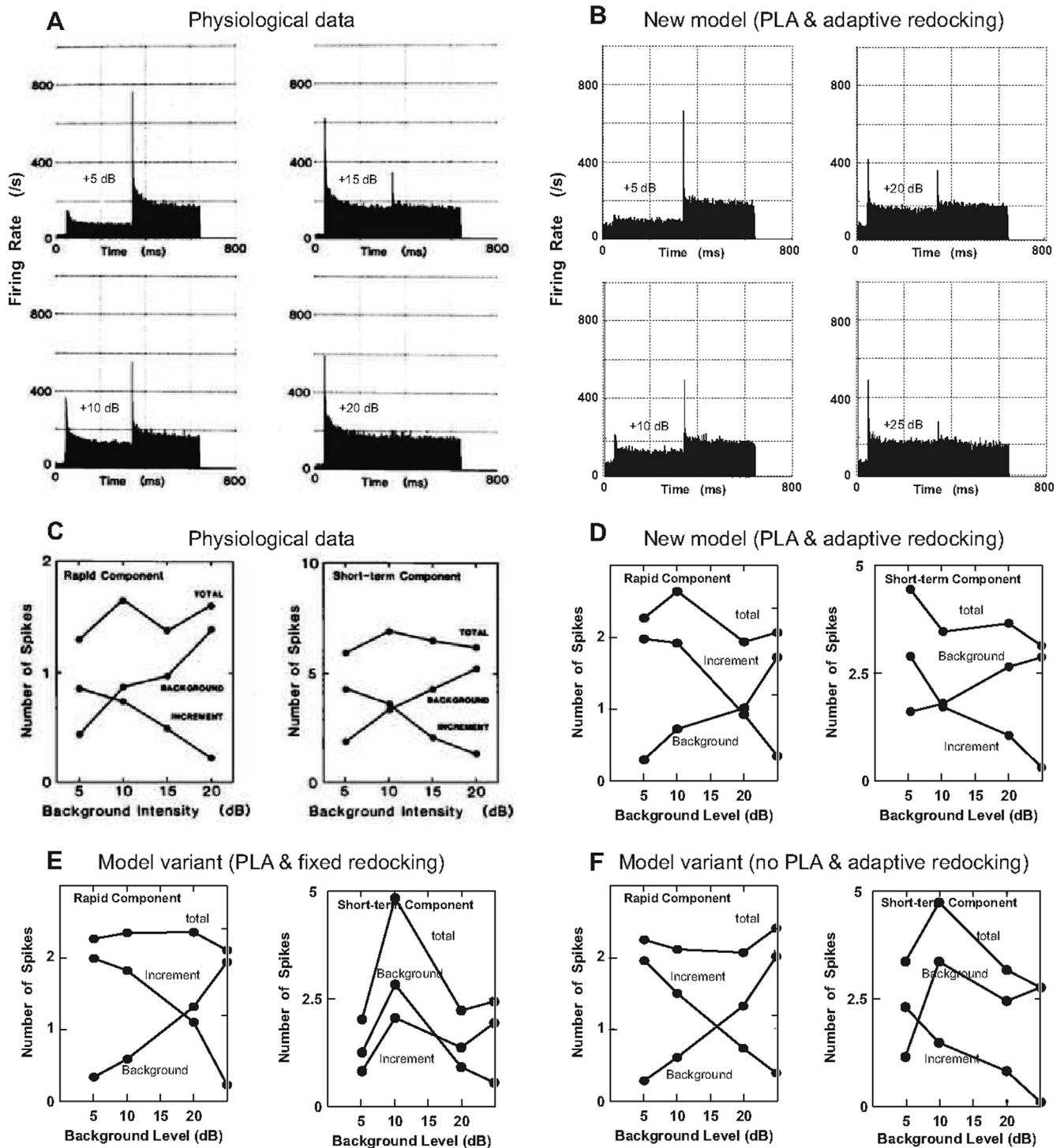


Fig. 4. ANF PSTHs and integrated transient response components for both rapid (~2 ms) and short-term (~60 ms) components for the amplitude increment response paradigm. Physiological responses from gerbil (Westerman and Smith, 1987) are shown in panels A and C, while panels B and D show predictions from the new model, and panels E and F show integrated response plots for two model variants. The stimulus was at CF (5.99 kHz for the example PSTHs), with a duration of 600 ms. The initial (“background”) levels of the tone were 5, 10, 15 and 20 dB above threshold. At 300 ms, the intensity was increased to 43 dB above threshold (increment) in all cases. A: Mongolian gerbil ANF PSTHs (binwidth of 2 ms) from Westerman and Smith (1987), reprinted with permission from the Acoustical Society of America (© 1987). B: Model histograms using the same paradigm as above, except that the highest level of the background tone was 25 dB above threshold because the model fiber shows a wider dynamic range than the corresponding AN fiber of the physiological data. C: Mean values of rapid and short-term “integrated transient response components” from six fibers from Westerman and Smith (1987), reprinted with permission from the Acoustical Society of America (© 1987). These integrated components are obtained by fitting each onset response of the PSTH with a function with a steady-state component and two exponential components and multiplying the firing rates of the fitted exponentials by their time constants. The curves indicate the integrated components for the background (initial) onset response, increment onset response, and their total, as labeled. D: Average model transient responses for 6 model ANFs using the same method as employed in the data. E: Predictions from a version of the model with fixed ($t_{rd} = 16$ ms) rather than adaptive redocking. F: Predictions from a version of the model without power-law adaptation (PLA).

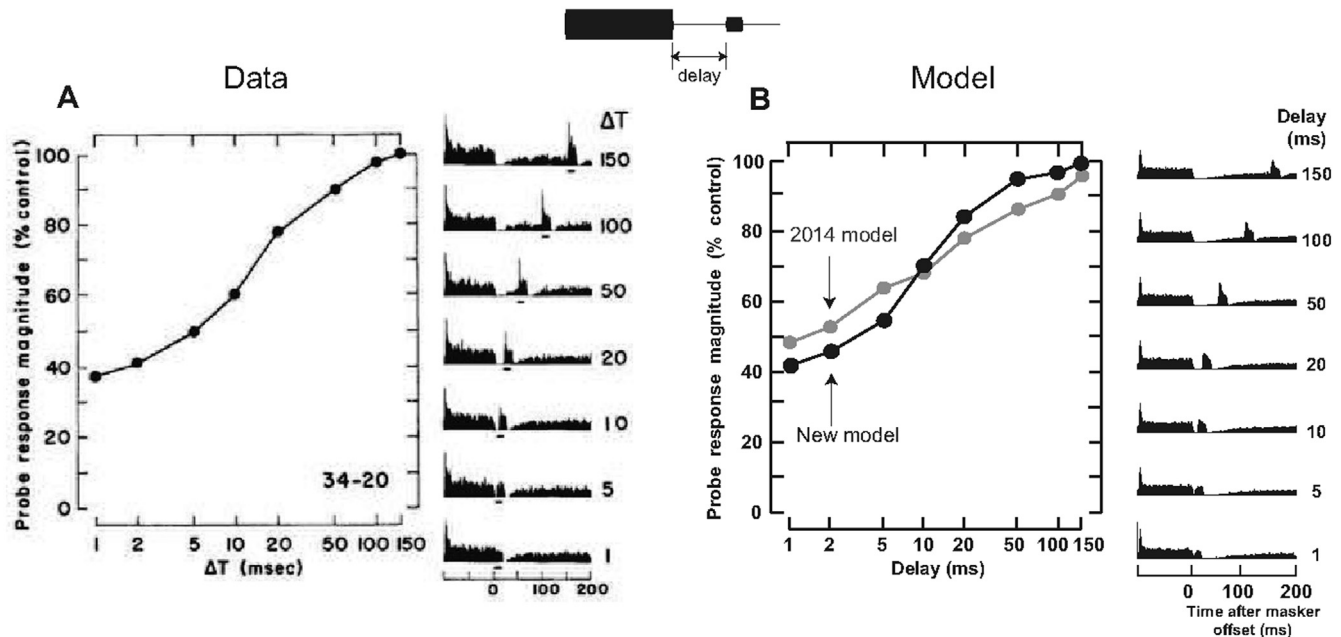


Fig. 5. Physiological forward-masking data (A panels) for an example ANF from Harris and Dallos (1979) and simulation results (B panels) for the 2014 and new models. Masker tone at 30 dB above threshold and probe tone at 20 dB re. threshold. Data reprinted from Harris and Dallos (1979) with permission from the American Physiological Society (© 1979).

permitted a single value of the parameter SR to be set for each spont rate class in the model while still allowing the spread of *measured* spont rates for each model class to be caused by the fluctuations in the fGn, as first proposed by Jackson and Carney (2005). However, a side-effect of producing the spread in spont rate via the fGn is that rate-level functions generated with the 2009/2014 model tend to be clustered together for each spont rate class, as shown in Fig. 7A, rather than having a continuum of thresholds that are negatively correlated to the logarithm of the spont rate as observed in the physiological data (see Fig. 7C). As shown in Fig. 7, the new model has a more physiological continuum of rate-level functions (panel B) with the appropriate dependence of the threshold on the spont rate (panel D). This is achieved via the combined effect of: i) reducing the standard deviation of the fGn, ii) making the input nonlinearity of the PLA vary systematically with SR as given in (1)–(6), and iii) having a distribution of values of the parameter SR as given in Table 1. Comparisons of the new model's spont-rate histogram and saturated firing rate as a function of CF to published data are also provided in the Supplementary Material.

The Fano factor quantifies the irregularity of spiking according to:

$$F(T) = \text{var}[N(T)]/E[N(T)] \quad (29)$$

where $N(T)$ is the number of spikes in the time period T , $\text{var}[\cdot]$ is the variance, and $E[\cdot]$ is the mean. A Poisson process has a Fano factor of 1, while values less than 1 indicate more regular firing (lower variance) than a Poisson process and values greater than 1 indicate more irregular firing (higher variance). Fig. 8 compares the model Fano factor behavior to data from an example ANF from Peterson et al. (2014). The data exhibit a dip in the Fano factor for a counting interval T around 100 ms, and the dip is somewhat deeper than is obtained if the interspike intervals are randomly shuffled, indicating that the drop in the irregularity of firing is more than can be explained by refractoriness alone. For counting intervals above 100 ms, the Fano factor then grows steeply as a function of T such that it exceeds a value of 1. A Fano factor above 1 corresponds to more irregular firing than a Poisson process, which can be produced

by slow fluctuations in the firing rate or bursting in the spike train. The Fano factor for the 2014 model (gray curves in Fig. 8) has a dip at 10 ms (rather than 100 ms), and the depth of the dip can be fully explained by refractoriness, as illustrated by the Fano factor for the shuffled spike train (gray dashed curve) at a counting interval of 10 ms. The Fano factor then grows rapidly with increasing T such that it is substantially larger than that observed in the data. This increase is caused by the fGn in the PLA of the synapse model, and as mentioned previously, the standard deviation for the fGn was set to too large a value in the 2009/2014 model. The new model (black curves) correctly shows a dip at the correct value of $T = 100$ ms that is greater than can be explained by refractoriness, and grows to more correct magnitudes for longer counting intervals.

Another method for quantifying how spike trains deviate from a renewal process with a constant rate is to compute the serial interspike interval correlation coefficient (SIICC), which measures the interdependence of N consecutive ISIs according to:

$$\rho = \frac{(N-2)^{-1} \sum_{i=1}^{N-1} (ISI_i - E[ISI])(ISI_{i+1} - E[ISI])}{(N-1)^{-1} \sum_{i=1}^N (ISI_i - E[ISI])^2} \quad (30)$$

The left-hand panel of Fig. 9 shows the SIICCs computed from the spontaneous activity of a population of ANFs reported in Peterson et al. (2014). Renewal processes have an SIICC of zero, while positive SIICC values correspond to cases where ISIs shorter than the mean tend to be clustered in time and ISIs longer than the mean tend to be similarly clustered (which can occur due to fluctuations in the firing rate over the duration of a spike train), and negative values indicate situations where short and long ISIs tend to alternate. In the example data, it can be observed that the majority of SIICC values are negative for short mean ISIs, with a minority of positive values, and the SIICC tends towards zero for longer mean ISIs. Peterson and Heil (In Press) argue that the positive SIICC values for short mean ISI observed in a subset of fibers is due to incomplete recovery from preceding acoustic stimulation, which was applied in their data collection in addition to their recording of spontaneous activity. The 2014 model (gray symbols

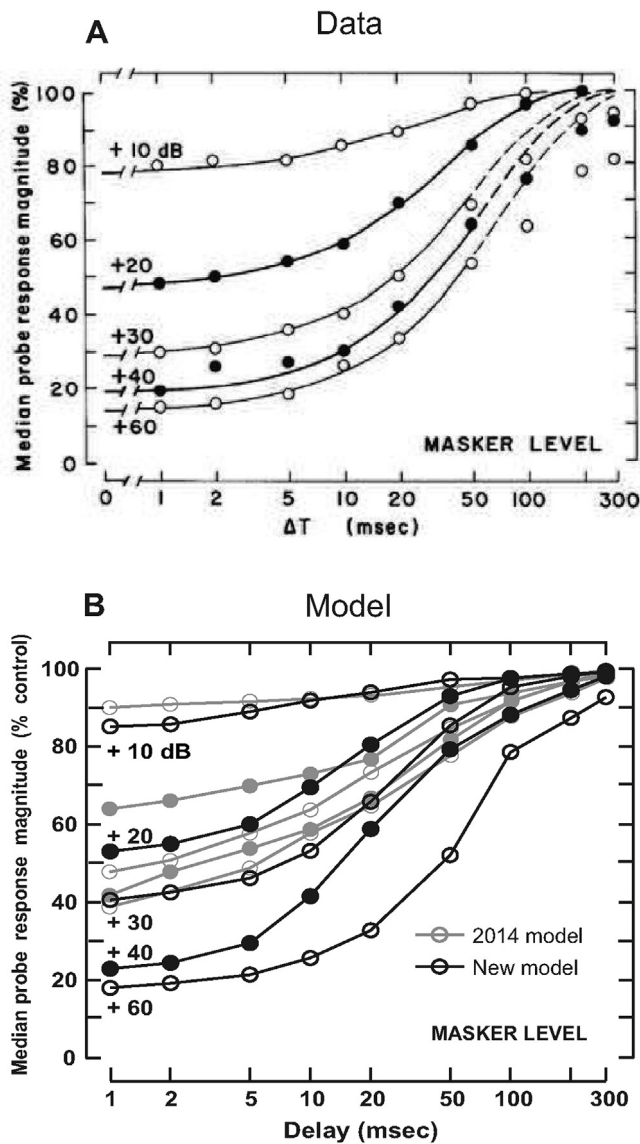


Fig. 6. Median ANF forward-masking curves at a range of masker levels for (A) a population of ANFs from Harris and Dallos (1979) and (B) simulation results for the 2014 and new models. Probe tone at 20 dB re. threshold and masker level as labeled. Data reprinted from Harris and Dallos (1979) with permission from the American Physiological Society (© 1979).

and curve in right-hand panel) tends to have only positive SIIC values, due to the overly strong fGn and the renewal-process spike generation approach in the old model. In contrast, the new model (black symbols and curve in the right-hand panel of Fig. 9) correctly predicts the trend exhibited by the data. As explained by Peterson et al. (2014), the negative correlation in consecutive ISIs occurs when there is a limited number of docking sites because after a short ISI it is more likely that at least two docking sites need to be replenished (i.e., vesicle redocking) before they are available for release again, such that the next ISI is likely to be longer, while after a long ISI it is more likely that only one docking site needs to be replenished, so the next ISI can be shorter. At longer mean ISIs, there is more time for redocking to occur at all release sites, such that the consecutive ISIs become uncorrelated and the SIIC approaches zero.

The results for the Fano factor and SIIC demonstrate that the release-redocking mechanism and the fGn can have a substantial

effect on the spiking statistics within a spike train. However, the analytical approximation derived in Section 3 provides a prediction of the mean and variance in spike count across spike trains (for a particular ANF in response to repeated identical stimuli or for a population of identical fibers in response to the one stimulus) and should be accurate if $S_{out}(t)$ is known (as it includes the non-stationarity due to the fGn) and is not changing too rapidly. Fig. 10 shows the mean and variance in the spike count of an example high-CF model ANF as a function of time in response to a tone at the fiber's CF (8 kHz). Simulation results are shown for a set of spike trains analyzed with three different time bin sizes: A) 0.5 ms, B) 5 ms, and C) 50 ms. The PSTHs show the mean and variance in the spike count (top and bottom sub-panels, respectively), while the filled circles show the analytical approximations. The predictions of the mean count shown by the red filled circles are seen to be very accurate for all PSTH bin sizes, except for the onset response where $S_{out}(t)$ changes too rapidly for the approximation to be valid. As described by (26) and (27), the variance depends on the bin size (which is also captured by the Fano factor). The 0.5 ms bin size (panel A) is short enough that the variance in spike count is best predicted by Eq. (27) (blue filled circles), while the 50 ms bin size (panel C) is long enough that Eq. (26) (green filled circles) well describes the variances, and the variance in spike count for a 5 ms bin size (panel B) is between the two analytical approximations. Note that these approximations will be poorer for stimulus frequencies below 3 kHz, as synchronization in $S_{out}(t)$ to the stimulus periodicity will lead to rapid fluctuations that invalidate the assumption made in the derivation of the analytical approximations. Therefore, when using the model for signal detection theory applications that include stimulus components below 3 kHz, in addition to applications that require high accuracy in describing the spiking statistics within a spike train, it would be preferable to use the spike outputs rather than the analytical approximations.

As described in Section 2, the new model has only a shorter relative refractory component, because the longer recovery effect is now attributed to the replenishment time for the limited number of docking sites. In addition, the relative refractory period is made a function of the rate at which the synapse is driven, as described by (9), based on the observations of Li and Young (1993). In Fig. 11, simulation results for estimates of the relative refractory period of individual ANFs are compared to the published data of Li and Young (1993). Li and Young used a two-step fitting procedure where the absolute refractory period was first estimated from the ISI histogram and then a function was fit to the ISI histogram to estimate the relative refractory period (their Eq. (3)). We used the same approach to obtain estimates of the apparent relative refractory period based on this function fit. While the renewal process assumed by Li and Young (1993) in fitting their ISI data does not take into consideration the possibility of presynaptic depression due to a relatively long time for redocking of synaptic vesicles, their analysis does still provide a helpful experimental estimate of recovery properties. The data exhibit a drop in the apparent relative refractory period with shorter mean ISIs (left panel), which the 2014 model cannot explain (gray symbols in right panel). In contrast, the new model (black symbols in right panel) exhibits the appropriate dependence of the apparent relative refractory period on the mean ISI. Note that the model, in contrast to some of the ANFs in the data, does not produce mean ISIs below 4 ms for the stimulus paradigms described in Li and Young (1993). The model's minimum mean ISI is more consistent with the saturated firing rates observed in Liberman (1978), as shown in the Supplementary Material, and it is not immediately clear how to resolve the different saturated rates observed in the two data sets.

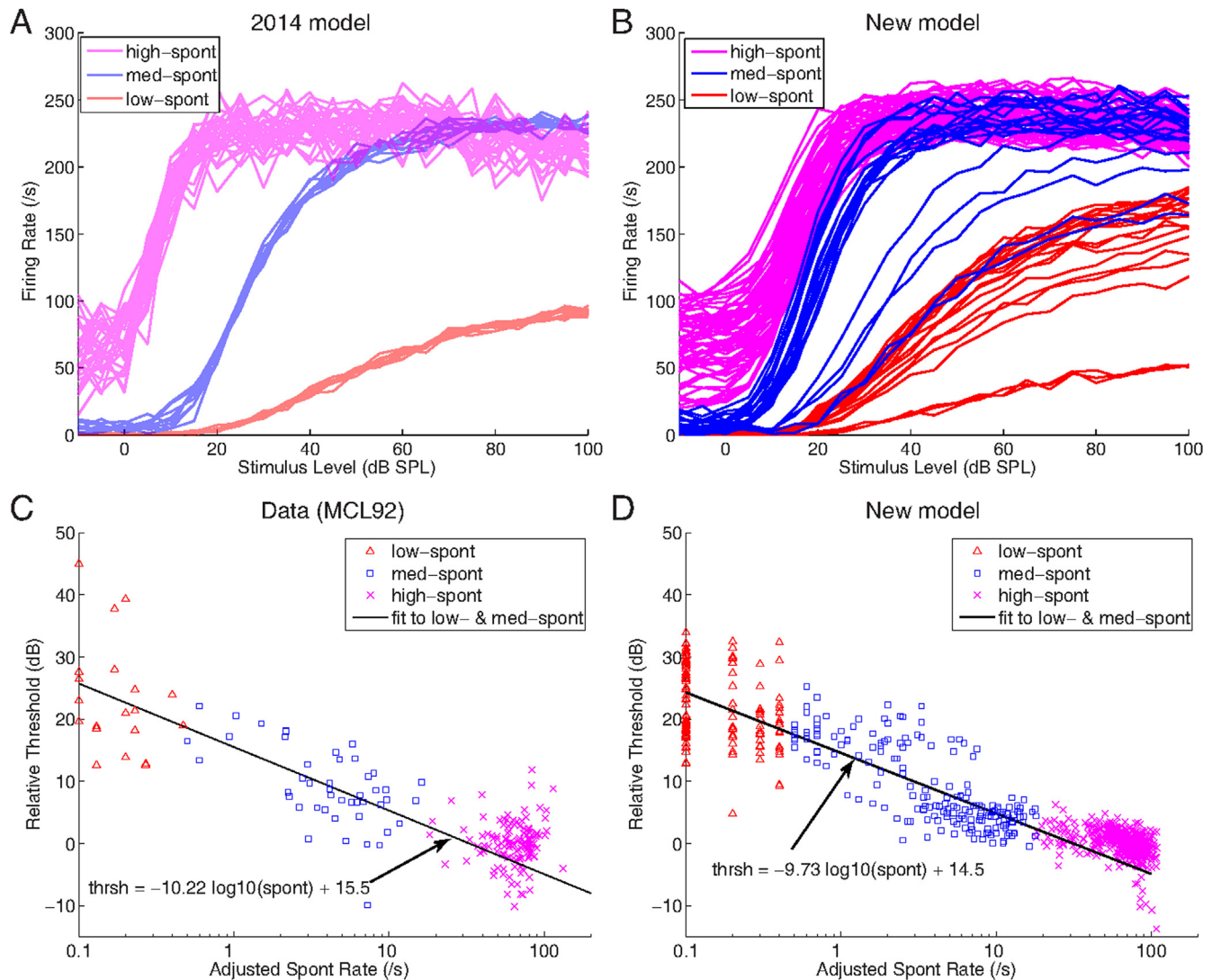


Fig. 7. Analysis of rate-level and threshold behavior as a function of spont rate. The top row shows rate-level functions for a population of high-CF model ANFs for: A) the 2014 model and B) the new model. CF = 8 kHz, 50-ms CF tone with 2.5-ms ramps and 50% duty cycle. The bottom row shows an analysis of how single ANF thresholds vary as a function of spont rate for: C) cat MCL92 from Liberman (1978) and D) the new model. The analysis follows that of Liberman (1978), except the spont rate values are plotted on a logarithmic scale and spont rate values below 0.1 (many having values of 0) are adjusted to have a value 0.1 to facilitate their inclusion in the fitting procedure. Thresholds are given relative to the mean absolute threshold for the high-spont fibers at each CF. Linear functions (on the log-spont scale) are fit to both the data and the simulation for the low- and med-spont ANFs, and extrapolations of these lines are seen to go through the clusters of high-spont values. The model fit is observed to be a good match to the data fit.

5. Discussion and conclusions

The primary goal of this study was to generalize the model of limited synaptic release sites from Peterson et al. (2014) and Peterson and Heil (In Press) to sound-driven activity and incorporate it into the auditory periphery model of Zilany et al. (2009, 2014) and to investigate how this affects the predictions of published data on ANF spiking statistics. In changing the synapse and spike-generation model structure to accomplish this (compare panels B and C of Fig. 2) and adjusting model parameters, it was also possible to correct the rate-level functions of the model (and their dependence on the SR) and further improve the model's predictions of physiological forward masking.

This latter improvement was achieved by moving the double-exponential adaptation previously obtained with the deterministic, continuous Westerman and Smith (1988) model placed before the power-law adaptation model to instead be described by the stochastic, quantal adaptive redocking mechanism after the PLA

section. When the Zilany et al. (2009) model was created, it was not clear whether to place the PLA section before or after the Westerman and Smith (1988) adaptation, i.e., whether the power-law behavior is generated pre- or post-synaptically. There are voltage-gated ion channels in ANFs that do lead to intrinsic adaptation and fluctuations in excitability when electrically stimulated (Boulet et al., 2016; Negm and Bruce, 2008, 2014; Boulet and Bruce, 2017), making postsynaptic PLA a distinct possibility. However, we have conducted preliminary simulations in which a Poisson process was used to drive conductance-based synaptic inputs to the biophysical ANF model of Negm and Bruce (2014), and the simulation results did *not* reproduce the Fano factor behavior observed in the spontaneous activity of ANFs (left panel of Fig. 8). Recently, Wu et al. (2016) have shown that ANF excitatory postsynaptic currents exhibit similar Fano factor versus time window behavior to ANF spikes, further supporting a synaptic origin of the non-stationarity. Thus, it now appears that the fluctuations in excitability are caused predominantly by presynaptic ion channel noise,

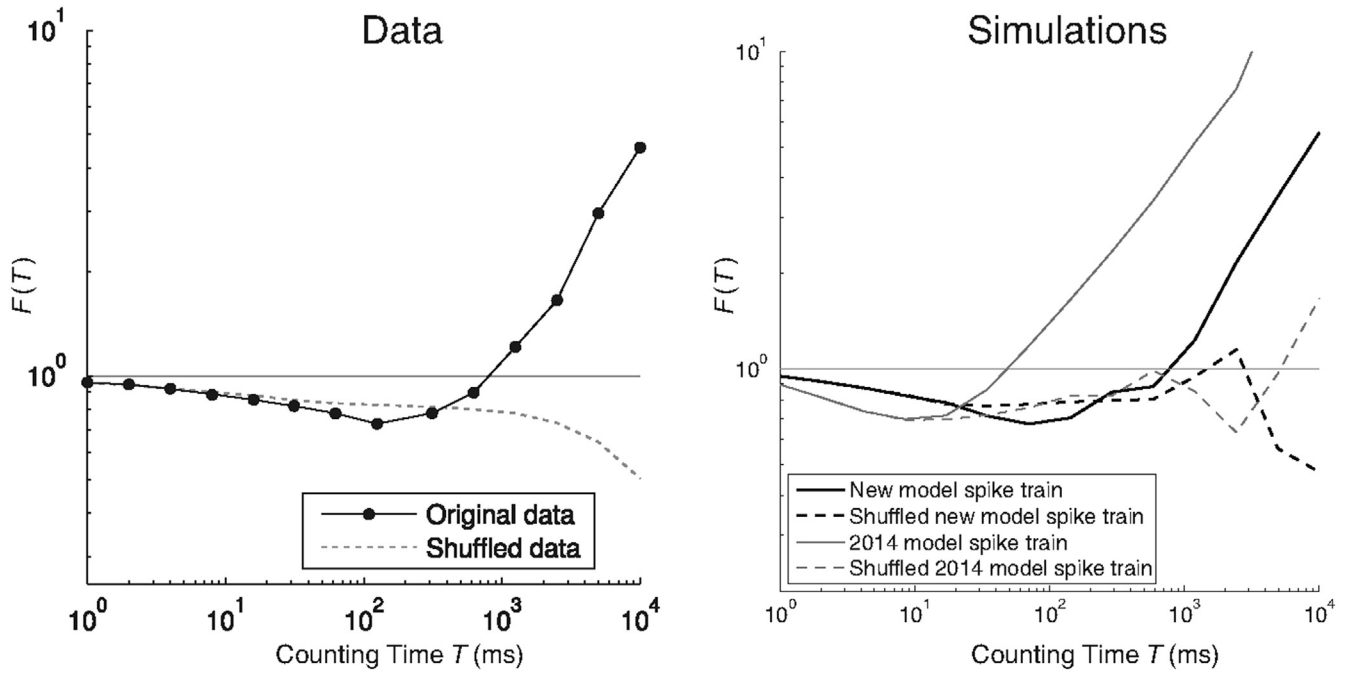


Fig. 8. The Fano factor as a function of counting time for an example high-spont ANF (left panel) from Peterson et al. (2014) and for the 2014 and new synapse models (right panel; CF = 1.5 kHz, SR = 50 /s, $t_{abs} = 0.6$ ms, $t_{rel} = 0.6$ ms). Fano factor curves computed after random shuffling of the interspike intervals (dashed curves) illustrate the behavior that can be explained by refractoriness alone. Data reprinted from Peterson et al. (2014) with permission from the Society for Neuroscience (© 2014).

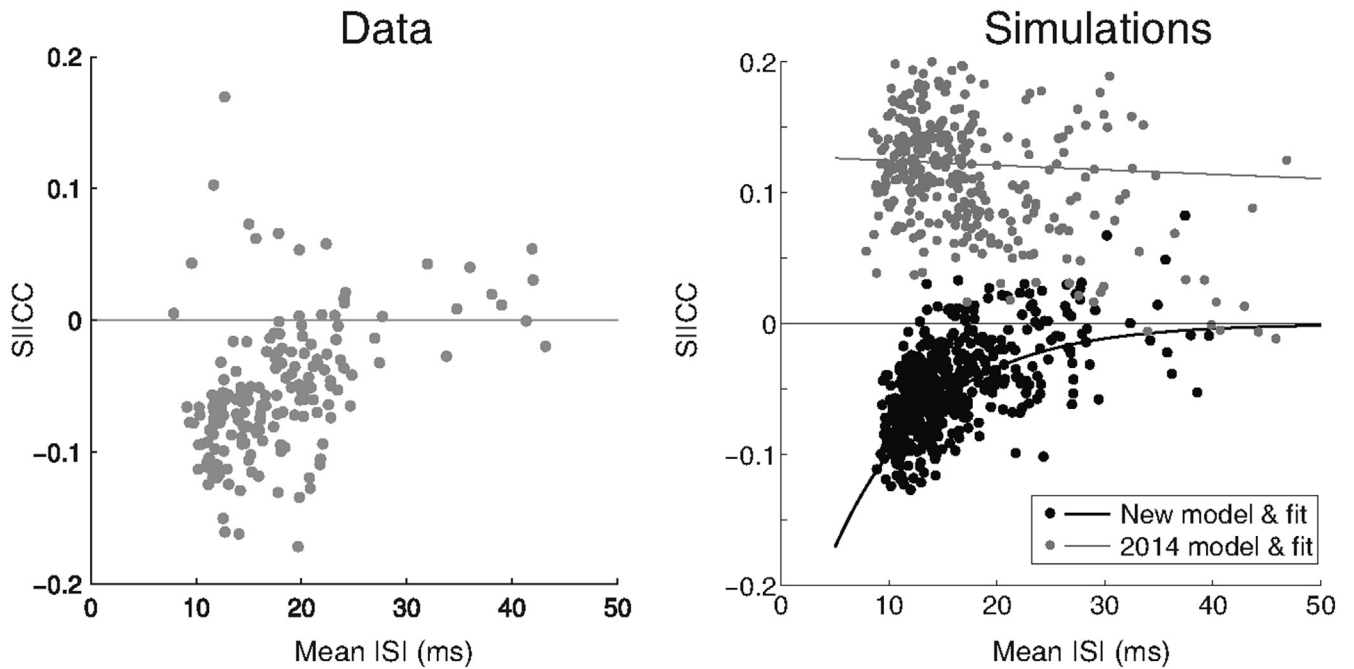


Fig. 9. The serial interspike interval correlation coefficient (SIICC) as a function of mean ISI for a sample of 180 ANF spontaneous spike trains (left panel) from Peterson et al. (2014) and for the 2014 and new synapse models (right panel). Data reprinted from Peterson et al. (2014) with permission from the Society for Neuroscience (© 2014).

as proposed by Moezzi et al. (2014, 2016), and presumably pre-synaptic ion channels also generate the PLA. This new model structure is thus much closer to the biophysical IHC-synapse models of Sumner et al. (2002), Meddis (2006) and Moezzi et al. (2014, 2016), however the proposed phenomenological model is simpler, is more computationally efficient, and has demonstrated power-law adaptation behavior.

Following Peterson et al. (2014) and Peterson and Heil (In Press), we have set the number of synaptic vesicle docking sites to 4 in all ANFs in the simulations presented in this study. However, the number of sites is a free parameter in the model code (as described in Section 2), although the derivation of the analytical approximation for the ISI distribution including refractoriness (see Section 3) becomes substantially more complicated for greater numbers of

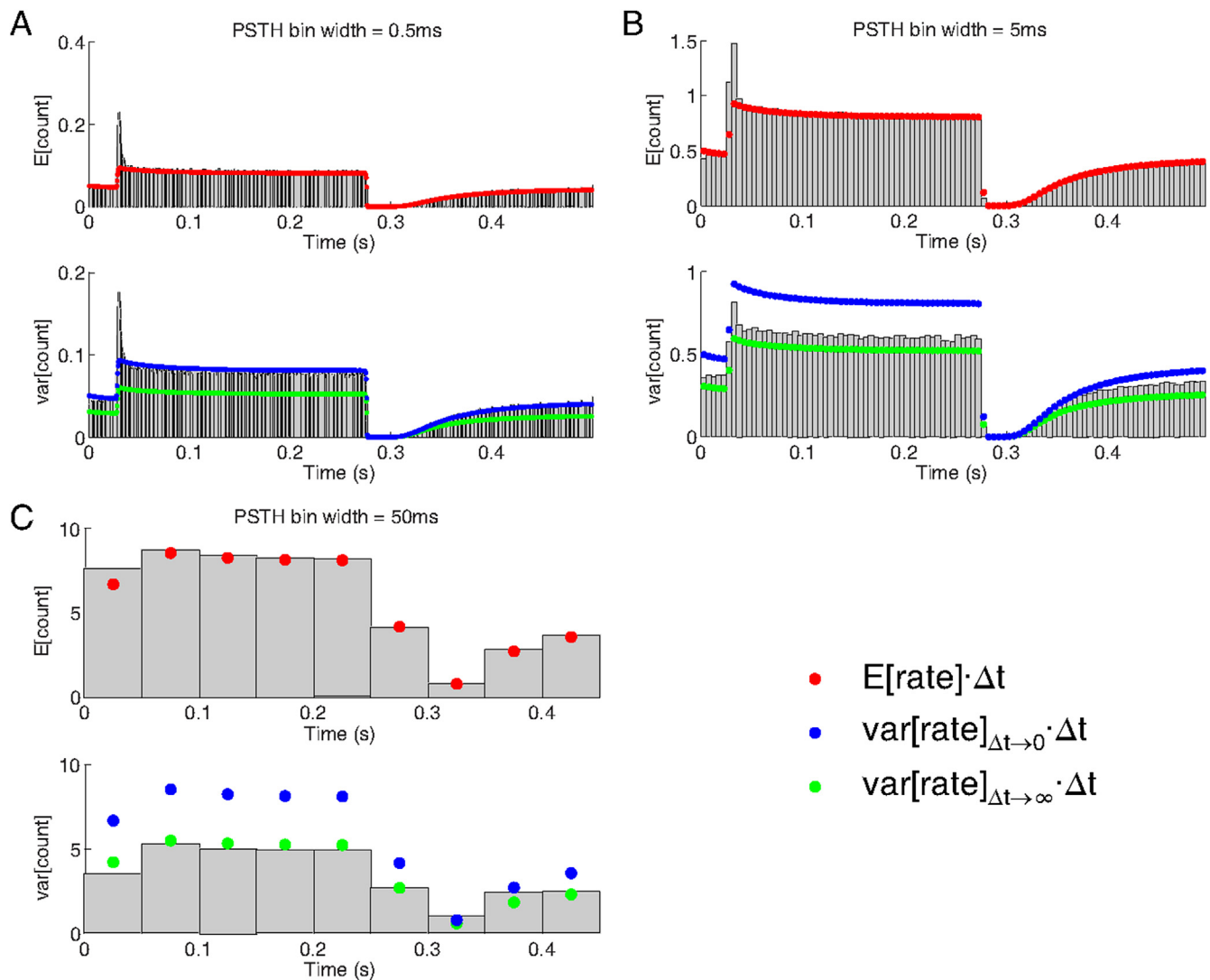


Fig. 10. Simulation results (histograms) and analytical approximations (filled circles) of the mean (top sub-panels) and variance (bottom sub-panels) in the spike count of an example high-spont, high-CF model ANF (CF = 8 kHz, SR = 100 /s, $t_{\text{abs}} = 0.6$ ms, $t_{\text{rel}} = 0.6$ ms) in response to a 250-ms long CF tone ($t = 25$ to 275 ms) with 2.5-ms ramps presented at 20 dB SPL. The mean and variance peri-stimulus time histograms (PSTHs) shown by the gray bars were obtained from spike trains generated from 10,000 trials. The PSTHs in panels A–C were constructed using the exact same spike trains but with different bin sizes (Δt): A) 0.5 ms, B) 5 ms, and C) 50 ms. The filled red circles in each panel shows the analytical predictions of the mean count PSTHs based on Eqs. (24) and (25). The filled blue circles show the analytical predictions of the variance in spike count for the case of $\Delta t \rightarrow 0$ based on Eqs. (27) and (28), while the filled green circles show the predictions of the variance for the case of $\Delta t \rightarrow \infty$ based on Eqs. (26) and (28).

release sites. Future investigations could consider whether there is a distribution of number of release sites across the population of ANFs, rather than all fibers having just 4. The analyses of Peterson et al. (2014) and Peterson and Heil (In Press) did show that very good prediction of their data could still be achieved across a range of values between ~ 3 and ~ 5 for the number of sites (and fairly good predictions over a slightly wider range). We have also run some preliminary simulations taking the synaptic events from the new auditory periphery model and using them to drive an updated biophysical ANF model (Boulet and Bruce, 2017) and have found that the Fano factor and SIICC predictions are not very sensitive to the number of release sites over the range 3–9 or to the size of the postsynaptic conductance changes triggered by synaptic releases, as long as some conductance changes are large enough to generate spikes in the ANF.

Peterson and Heil (In Press) argued that the standard deviation of the fGn in the Zilany et al. (2009, 2014) models was too large to accurately predict their Fano factor data when coupled with their

synapse model. We did indeed find in this study that we needed to reduce the standard deviation of the fGn in our new model, but not to the same degree as Peterson and Heil (In Press), because they passed the fGn directly into their synaptic release model, whereas in our model the fGn passes first through the slow PLA (see Fig. 2), which effectively low-pass filters the fGn and reduces its magnitude at the input to our synaptic release model.

In conclusion, we have found that incorporating a limited number of synaptic release sites with adaptive redocking dynamics produces improved predictions of both spontaneous and sound-driven ANF spiking statistics. Having correct ISI statistics in the model may be important for evaluating temporal coding theories (such as temporal pitch models) and for the response properties of cochlear nucleus neurons, particularly those receiving relatively few synaptic inputs from ANFs where the input ISI statistics may have greater impact. Other subsequent changes to the model structure and parameters also produce improved predictions of ANF rate-level functions and forward-masking behavior. While the

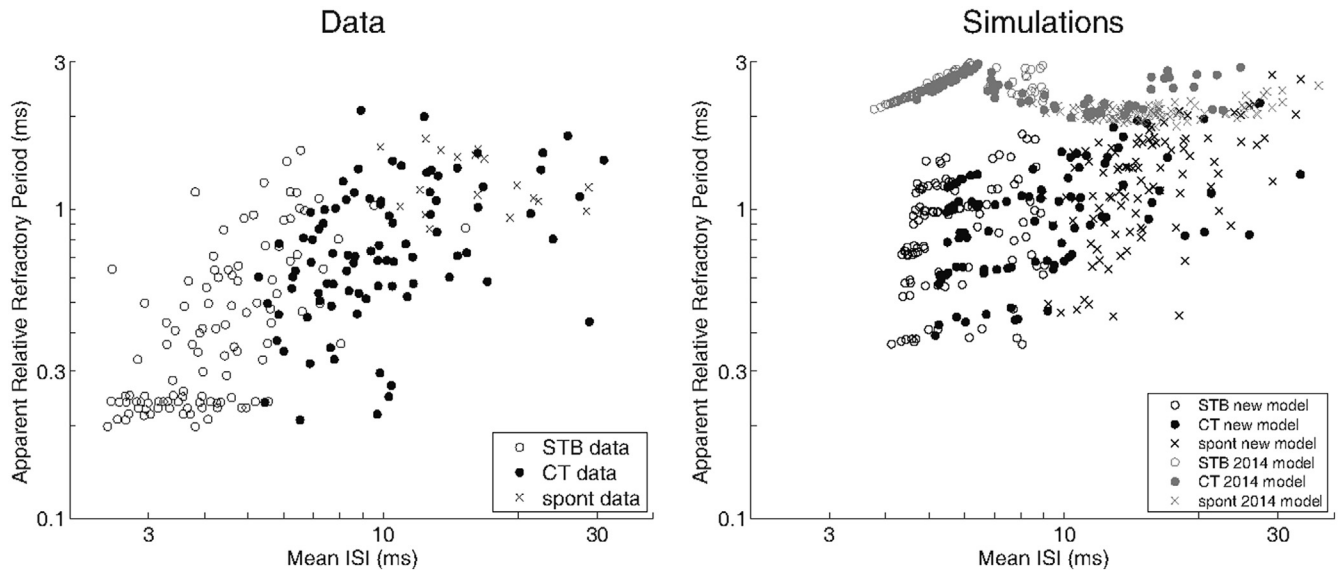


Fig. 11. Apparent relative refractory period versus mean ISI for a population of ANFs (left panel) from Li and Young (1993) and simulation results (right panel) with the 2014 and new models for the cases of short tone burst (STB) or continuous tone (CT) stimulation or spontaneous activity. The term “apparent relative refractory period” indicates that the statistical estimation method of Li and Young (1993) will incorporate the effects of the presynaptic vesicle release-redocking dynamics into the estimate of refractoriness. Data reprinted from Li and Young (1993) with permission from Elsevier (© 1993).

new model is somewhat more computationally complex than the previous version, the improved physiological accuracy will be important for considering many questions related to neural coding of sound in hearing research and related industrial application.

Acknowledgments

We thank Laurel Carney and Eric Young for helpful discussion about this work, Spencer Chambers and Laura Green for running the extra simulations described in the Discussion, the authors of the auditory nerve fiber data articles for sharing their figures and some data, Régis Nouvian for giving permission to use and adapt his synapse schematic, and the two reviewers for invaluable feedback. This research was supported by NSERC Discovery Grant #261736, the Atlantic Canada Opportunities Agency (ACOA) Innovative Communities Fund Project # 204210 and Business Development Program Project # 205595, the Excite Corporation, and the Government of Newfoundland and Labrador Regional Development Fund Ref # 30-11044-003.

Appendix A. Supplementary data

Supplementary data related to this article can be found at <https://doi.org/10.1016/j.heares.2017.12.016>.

References

- Boulet, J., Bruce, I.C., 2017. Predictions of the contribution of HCN half-maximal activation potential heterogeneity to variability in intrinsic adaptation of spiral ganglion neurons. *J. Assoc. Res. Otolaryngol* 18, 301–322. <https://doi.org/10.1007/s10162-016-0605-5>.
- Boulet, J., White, M.W., Bruce, I.C., 2016. Temporal considerations for stimulating spiral ganglion neurons with cochlear implants. *J. Assoc. Res. Otolaryngol* 17, 1–17. <https://doi.org/10.1007/s10162-015-0545-5>.
- Bruce, I.C., Sachs, M.B., Young, E.D., 2003. An auditory-periphery model of the effects of acoustic trauma on auditory nerve responses. *J. Acoust. Soc. Am.* 113, 369–388. <https://doi.org/10.1121/1.1519544>.
- Carney, L.H., 1993. A model for the responses of low-frequency auditory-nerve fibers in cat. *J. Acoust. Soc. Am.* 93, 401–417. <https://doi.org/10.1121/1.405620>.
- Cartee, L.A., van den Honert, C., Finley, C.C., Miller, R.L., 2000. Evaluation of a model of the cochlear neural membrane. I: Physiological measurement of membrane characteristics in response to intrameatal electrical stimulation. *Hear. Res.* 146, 143–152. [https://doi.org/10.1016/S0378-5955\(00\)00109-X](https://doi.org/10.1016/S0378-5955(00)00109-X).
- Cartee, L.A., Miller, C.A., van den Honert, C., 2006. Spiral ganglion cell site of excitation I: Comparison of scala tympani and intrameatal electrode responses. *Hear. Res.* 215, 10–21. <https://doi.org/10.1016/j.heares.2006.02.012>.
- Cox, D.R., Smith, W.L., 1954. On the superposition of renewal processes. *Biometrika* 41, 91–99. <https://doi.org/10.2307/2333008>.
- Drew, P.J., Abbott, L.F., 2006. Models and properties of power-law adaptation in neural systems. *J. Neurophysiol.* 96, 826–833. <https://doi.org/10.1152/jn.00134.2006>.
- Gaumond, R.P., Kim, D.O., Molnar, C.E., 1983. Response of cochlear nerve fibers to brief acoustic stimuli: role of discharge-history effects. *J. Acoust. Soc. Am.* 74, 1392–1398. <https://doi.org/10.1121/1.390164>.
- Gaumond, R.P., Molnar, C.E., Kim, D.O., 1982. Stimulus and recovery dependence of cat cochlear nerve fiber spike discharge probability. *J. Neurophysiol.* 48, 856–873.
- Harris, D.M., Dallos, P., 1979. Forward masking of auditory nerve fiber responses. *J. Neurophysiol.* 42, 1083–1107.
- Heinz, M.G., Colburn, H.S., Carney, L.H., 2002. Quantifying the implications of nonlinear cochlear tuning for auditory-filter estimates. *J. Acoust. Soc. Am.* 111, 996–1011. <https://doi.org/10.1121/1.1436071>.
- Heinz, M.G., Zhang, X., Bruce, I.C., Carney, L.H., 2001. Auditory nerve model for predicting performance limits of normal and impaired listeners. *ARLO* 2, 91–96. <https://doi.org/10.1121/1.1387155>.
- Jackson, B.S., Carney, L.H., 2005. The spontaneous-rate histogram of the auditory nerve can be explained by only two or three spontaneous rates and long-range dependence. *J. Assoc. Res. Otolaryngol* 6, 148–159. <https://doi.org/10.1007/s10162-005-5045-6>.
- Johnson, D., Swami, A., 1983. The transmission of signals by auditory-nerve fiber discharge patterns. *J. Acoust. Soc. Am.* 74, 493–501. <https://doi.org/10.1121/1.389815>.
- Kiang, N.Y.S., 1965. *Discharge Patterns of Single Fibers in the Cat's Auditory Nerve*. Res. Monogr. No. 35. M.I.T. Press, Cambridge, MA.
- Li, J., Young, E.D., 1993. Discharge-rate dependence of refractory behavior of cat auditory-nerve fibers. *Hear. Res.* 69, 151–162. [https://doi.org/10.1016/0378-5955\(93\)90103-8](https://doi.org/10.1016/0378-5955(93)90103-8).
- Liberman, M.C., 1978. Auditory nerve response from cats raised in a low noise chamber. *J. Acoust. Soc. Am.* 63, 442–455. <https://doi.org/10.1121/1.381736>.
- Lowen, S.B., Teich, M.C., 1992. Auditory-nerve action potentials form a nonrenewal point process over short as well as long time scales. *J. Acoust. Soc. Am.* 92, 803–806. <https://doi.org/10.1121/1.403950>.
- Meddis, R., 2006. Auditory-nerve first-spike latency and auditory absolute threshold: a computer model. *J. Acoust. Soc. Am.* 119, 406–417. <https://doi.org/10.1121/1.2139628>.
- Miller, C.A., Abbas, P.J., Robinson, B.K., 2001. Response properties of the refractory auditory nerve fiber. *J. Assoc. Res. Otolaryngol* 2, 216–232. <https://doi.org/10.1007/s101620010083>.
- Moezzi, B., Iannella, N., McDonnell, M.D., 2014. Modeling the influence of short term depression in vesicle release and stochastic calcium channel gating on auditory nerve spontaneous firing statistics. *Front. Comput. Neurosci.* 8 <https://doi.org/10.3389/fncom.2014.00163>.

- Moezzi, B., Iannella, N., McDonnell, M.D., 2016. Ion channel noise can explain firing correlation in auditory nerves. *J. Comput. Neurosci.* 41, 193–206. <https://doi.org/10.1007/s10827-016-0613-9>.
- Negm, M.H., Bruce, I.C., 2008. Effects of I_h and I_{KLT} on the response of the auditory nerve to electrical stimulation in a stochastic Hodgkin–Huxley model. In: *Proceedings of 30th Annual International Conference of the IEEE Engineering in Medicine and Biology Society (EMBC2008)*. IEEE, Piscataway, NJ, pp. 5539–5542. <https://doi.org/10.1109/IEMBS.2008.4650469>.
- Negm, M.H., Bruce, I.C., 2014. The effects of HCN and KLT ion channels on adaptation and refractoriness in a stochastic auditory nerve model. *IEEE Trans. Biomed. Eng.* 61, 2749–2759. <https://doi.org/10.1109/tbme.2014.2327055>.
- Peterson, A.J., Heil, P., 2017. A simple model of the inner-hair-cell ribbon synapse accounts for mammalian auditory-nerve-fiber spontaneous spike times. *Hear. Res.* <https://doi.org/10.1016/j.heares.2017.09.005> (in press).
- Peterson, A.J., Irvine, D.R.F., Heil, P., 2014. A model of synaptic vesicle-pool depletion and replenishment can account for the interspike interval distributions and nonrenewal properties of spontaneous spike trains of auditory-nerve fibers. *J. Neurosci.* 34, 15097–15109. <https://doi.org/10.1523/jneurosci.0903-14.2014>.
- Safieddine, S., El-Amraoui, A., Petit, C., 2012. The auditory hair cell ribbon synapse: from assembly to function. *Annu. Rev. Neurosci.* 35, 509–528. <https://doi.org/10.1146/annurev-neuro-061010-113705>.
- Sumner, C.J., O'Mard, L.P., Lopez-Poveda, E.A., Meddis, R., 2002. A revised model of the inner-hair-cell and auditory nerve complex. *J. Acoust. Soc. Am.* 111, 2178–2188. <https://doi.org/10.1121/1.1453451>.
- Tan, Q., Carney, L.H., 2003. A phenomenological model for the responses of auditory-nerve fibers. II. Nonlinear tuning with a frequency glide. *J. Acoust. Soc. Am.* 114, 2007–2020. <https://doi.org/10.1121/1.1608963>.
- Teich, M.C., 1989. Fractal character of the auditory neural spike train. *IEEE Trans. Biomed. Eng.* 36, 150–160. <https://doi.org/10.1109/10.16460>.
- Teich, M.C., Johnson, D.H., Kumar, A.R., Turcott, R.G., 1990. Rate fluctuations and fractional power-law noise recorded from cells in the lower auditory pathway of the cat. *Hear. Res.* 46, 41–52. [https://doi.org/10.1016/0378-5955\(90\)90138-f](https://doi.org/10.1016/0378-5955(90)90138-f).
- Teich, M.C., Khanna, S.M., 1985. Pulse-number distribution for the neural spike train in the cat's auditory nerve. *J. Acoust. Soc. Am.* 77, 1110–1128. <https://doi.org/10.1121/1.392176>.
- Torab, P., Kamen, E.W., 2001. On approximate renewal models for the superposition of renewal processes. In: *IEEE International Conference on Communications, 2001 (ICC 2001)*, pp. 2901–2906. <https://doi.org/10.1109/ICC.2001.936680>.
- Westerman, L.A., Smith, R.L., 1987. Conservation of adapting components in auditory-nerve responses. *J. Acoust. Soc. Am.* 81, 680–691. <https://doi.org/10.1121/1.394836>.
- Westerman, L.A., Smith, R.L., 1988. A diffusion model of the transient response of the cochlear inner hair cell synapse. *J. Acoust. Soc. Am.* 83, 2266–2276. <https://doi.org/10.1121/1.396357>.
- Wu, J.S., Young, E.D., Glowatzki, E., 2016. Maturation of spontaneous firing properties after hearing onset in rat auditory nerve fibers: spontaneous rates, refractoriness, and interfiber correlations. *J. Neurosci.* 36, 10584–10597. <https://doi.org/10.1523/JNEUROSCI.1187-16.2016>.
- Zhang, X., Heinz, M.G., Bruce, I.C., Carney, L.H., 2001. A phenomenological model for the responses of auditory-nerve fibers: I. Nonlinear tuning with compression and suppression. *J. Acoust. Soc. Am.* 109, 648–670. <https://doi.org/10.1121/1.1336503>.
- Zilany, M.S.A., Bruce, I.C., 2006. Modeling auditory-nerve responses for high sound pressure levels in the normal and impaired auditory periphery. *J. Acoust. Soc. Am.* 120, 1446–1466. <https://doi.org/10.1121/1.2225512>.
- Zilany, M.S.A., Bruce, I.C., 2007. Representation of the vowel /e/ in normal and impaired auditory nerve fibers: model predictions of responses in cats. *J. Acoust. Soc. Am.* 122, 402–417. <https://doi.org/10.1121/1.2735117>.
- Zilany, M.S.A., Bruce, I.C., Carney, L.H., 2014. Updated parameters and expanded simulation options for a model of the auditory periphery. *J. Acoust. Soc. Am.* 135, 283–286. <https://doi.org/10.1121/1.4837815>.
- Zilany, M.S.A., Bruce, I.C., Nelson, P.C., Carney, L.H., 2009. A phenomenological model of the synapse between the inner hair cell and auditory nerve: long-term adaptation with power-law dynamics. *J. Acoust. Soc. Am.* 126, 2390–2412. <https://doi.org/10.1121/1.3238250>.